Polymer 50 (2009) 4895–4905

Contents lists available at ScienceDirect

Polymer

journal homepage: www.elsevier.com/locate/polymer

Toughening mechanisms in epoxy–silica nanocomposites (ESNs)

Y.L. Liang, R.A. Pearson*

Center for Polymer Science and Engineering, Lehigh University, 5 East Packer Ave, Bethlehem, PA 18015-3195, USA

ARTICLE INFO

Article history:
Received 27 March 2009
Received in revised form
5 August 2009
Accepted 11 August 2009
Available online 14 August 2009

Keywords:
Nanocomposites
Nanosilica
Toughening mechanism

ABSTRACT

Two types of nanosilica (NS) particles with different average particle sizes (20 nm and 80 nm in diameter, respectively) were used to fabricate epoxy–silica nanocomposites (ESNs) in this study. No significant differences in fracture behavior were observed between the epoxies filled with 20 nm NS particles and the epoxies filled with 80 nm NS particles. Interestingly, both types of NS particles were found to be more efficient in toughening epoxies than micron size glass spheres. As with micron size glass spheres, the fracture toughness of the ESNs were affected by the crosslink density of the epoxy matrix, i.e. a lower crosslinked matrix resulted in a tougher ESN. The increases in toughness in both types of ESNs were attributed to a zone shielding mechanism involving matrix plastic deformation. Moreover, the use of Irwin's formalized plastic zone model precisely described the relationship between the fracture toughness, yield strength and the corresponding plastic zone size of the various ESNs examined.

1. Introduction

Rigid inorganic particles have been used to toughen epoxy resins for quite some time and such particles can provide modest improvements in fracture toughness [1–5]. In contrast to rubber-toughened epoxies, the use of inorganic rigid fillers provides toughened epoxies without a decrease in modulus [3]. Among the different types of inorganic fillers, micron size glass spheres have been a popular option since they are isotropic in shape, low cost, relatively stiff, and possess low coefficient of thermal expansion (CTE). CTE plays a critical role in alleviating the thermal stress between silicon chips and organic substrates when applied in microelectronic packaging [6].

Recently, a significant amount of fracture toughness improvement has been reported when mono-dispersed, non-agglomerated nanosilica (NS) particles, developed from sol–gel technology [7], are mixed into an epoxy resin [8–12]. The toughening mechanism of epoxy–silica nanocomposites (ESNs) proposed by Johnsen et al. [12] involves plastic void growth around debonded particles. Their quantitative model predicts that the improvement in fracture energy with increasing NS content and correlates well with experimental data. Interestingly, the effect of NS particle size and matrix crosslink density on fracture toughness has not been emphasized in the open literature. Also, it is of a great interest to enhance our comprehension of the toughening mechanisms in ESNs. In order to do so, a concise review of the toughening mechanisms in epoxy resins induced by micron-size glass spheres and nanometer-size silica is presented in the following paragraphs.

Researchers have used various models to predict the increases in toughness in filled epoxy systems including crack front pinning/particle bridging [13], crack path deflection [5], and microcracking [14]. Most glass bead filled epoxies systems possess several types of toughening mechanisms and the exact contribution of each type of toughening mechanism on the overall toughness is difficult to quantify. In the crack pinning concept [15], well-bonded inclusions locally pin the crack front and result in additional line tension in the crack front bowing between particles. Consequently, more energy is required to propagate the crack past inclusions. This model reveals that the relative improvement in the fracture toughness ($K_{composite}/K_{matrix}$) is a function of the filler volume fraction and particle diameter. On the other hand, for a weakly bonded inclusion, the crack front is deflected by the particle as a result of the tendency of crack to propagate towards the weak particle–matrix interface [5]. The fracture toughness improvement due to crack deflection is usually expressed as a function of fracture surface roughness as well as particle diameter. In the particle-induced microcracking concept [14], strain energy is absorbed when particles debond and concomitant matrix microcracking occurs. It is noteworthy that crack pinning and crack path deflection models predict increasing toughness with increasing particle size whereas the microcracking model favors smaller particles.

In contrast to the conventional wisdom obtained from previous micron-glass-sphere studies, Zhang [9] indicated that the advantages of ESNs are based on the larger amount of the interphase

* Corresponding author. Tel.: +1 610 758 3857; fax: +1 610 758 4244.
E-mail address: rp02@lehigh.edu (R.A. Pearson).

0032-3861/$ – see front matter © 2009 Published by Elsevier Ltd.
doi:10.1016/j.polymer.2009.08.014

Table 1
The formulations of ESNs investigated in this work.

ESNs					
NS (g)	1.9	3.8	7.5	15.0	37.5
Epoxy (g)	141	138.6	136.3	127.5	107.3
Piperidine (g)	7.1	6.9	6.8	6.4	5.4
Total Weight (g)	149.9	149.3	150.6	148.9	150.2
NS Content (wt%)	1.3%	2.5%	5.0%	10.1%	24.6%
NS Content (vol%)	0.8%	1.6%	3.2%	6.6%	17.4%

polymer layer and a shorter interparticle distance. The surfaces of modified NS particles develop an interphase polymer layer around the inclusion, which exhibits dissimilar mechanical properties compared with bulk composites [16]. By increasing the NS fraction, the interparticle distance is diminished to a level where the properties of the interphase polymer layer become significant enough to affect the performance of the bulk materials. In Zhang's study [9], the fracture behavior and flexural modulus were considerably improved when interparticle distance is smaller than the particle diameter. According to Zhang, smaller NS particles are more efficient toughening particles than traditional micron size particles used in epoxy resins.

The objective in this study is to investigate the influence of nanosilica (NS) particle size and matrix crosslink density on the toughening efficiency of epoxy–silica nanocomposites (ESNs). In addition to quantify the toughness, the mechanisms responsible for increasing the toughness of ESNs are also explored.

2. Experimental approach

2.1. Materials

Two different size nanosilica (NS) particles, nominal 20 nm and 80 nm in diameter, were examined: 20 nm (Nanopox E430, Nanoresins) and 80 nm (3 M) NS particles were dispersed in diglycidyl ether of bisphenol A/F (DGEBA/F), and DGEBA epoxy resin as received, respectively. Both NS particles were supplied as concentrated dispersions, therefore, a DGEBA epoxy resin (DER331, Dow Chemical, Co.) was used to adjust the NS fraction from 0.8 to 17.4 vol%. The mixing process consisted of mechanical stirring (120 rpm) at 80 °C under a vacuum. After 4 h of mixing, 5 phr (per hundred parts resin) curing agent (piperidine, Aldrich) was added and stirred for another 10 min under atmospheric pressure. Then the mixture was poured out into a pre-heated steel mold with Teflon base release agent sprayed on it. The curing schedule for the study on the effect of NS particle size on mechanical properties was 160 °C for 6 h. However, in order to investigate the effect of matrix crosslink density, two other cure schedules (80 °C for 24 h and 120 °C for 16 h) were also applied and these results are discussed in Section 3.5.

The formulations of ESNs investigated are shown in Table 1. The volume fractions of NS particles were estimated according to the weight ratio of each component and the material densities obtained from the manufacturers and the reference (DGEBA: 1.16 g/cm^3; NS: 1.8 g/cm^3 [12], and piperidine: 0.86 g/cm^3). In order to simplify the calculation, it was assumed that the total volume of the ESN equals the sum of the volume from each component included in the blend.

2.2. Experimental methods

For the NS particle-dispersion study, the composite samples were sent to the Core Electron Microscopy Facility in UMass Medical School for transmission electron microscopy (TEM) investigation. The thickness of the TEM samples was maintained at 120 nm by cryomicrotoming at −10 °C.

The glass transition temperature, T_g, of cured epoxies was determined using the mid-point of the glass transition process according to the second scan from differential scanning calorimeter (DSC, model 2920, TA Instrument). The sample weight was 10–20 mg, and the heating rate was 10 °C/min.

A screw-driven material testing machine (model 5567, Instron) was used to characterize the mechanical properties of the materials studied under ambient temperature. Compression tests were conducted using ASTM D695 guidelines [17] with tetragonal shaped specimens of 5.0 mm × 5.0 mm × 10.0 mm and cross-head speed 1 mm/min. At least 5 samples for each formulation were tested. The compressive modulus and the yield stress were recorded for the calculations of the fracture energy and the plastic-zone size estimation. Note that we assumed that the compressive modulus is equivalent to the tensile modulus, i.e. Young's modulus.

The fracture toughness, K_{IC}, was measured according to ASTM D5045-99 guidelines under monotonic loading conditions [18]. A three point-bending (3PB) specimen was chosen with the following dimensions: 76.2 mm × 12.7 mm × 6.4 mm. At least 5 samples for

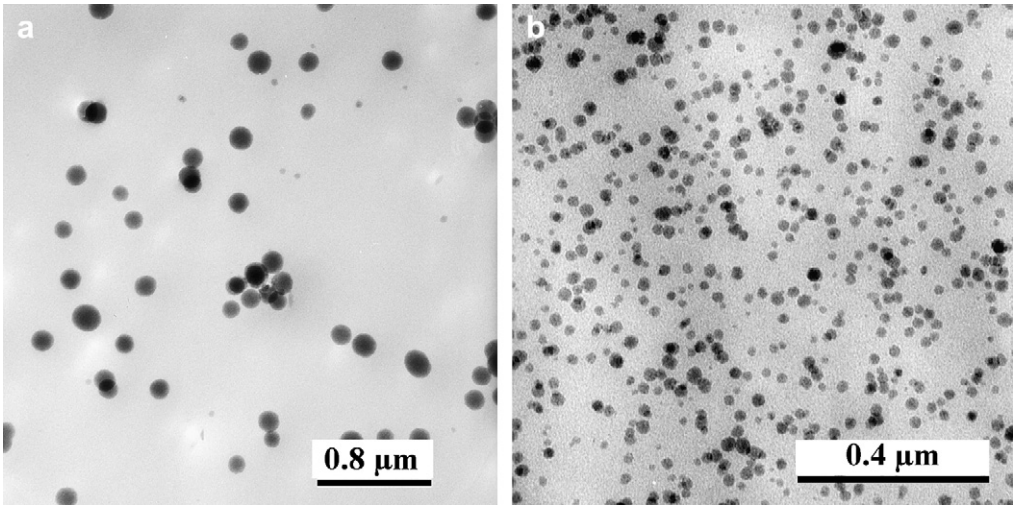

Fig. 1. TEM micrographs for particle-dispersion investigation in low NS content (3.2 vol %): (a) 80ESN, (b) 20ESN.

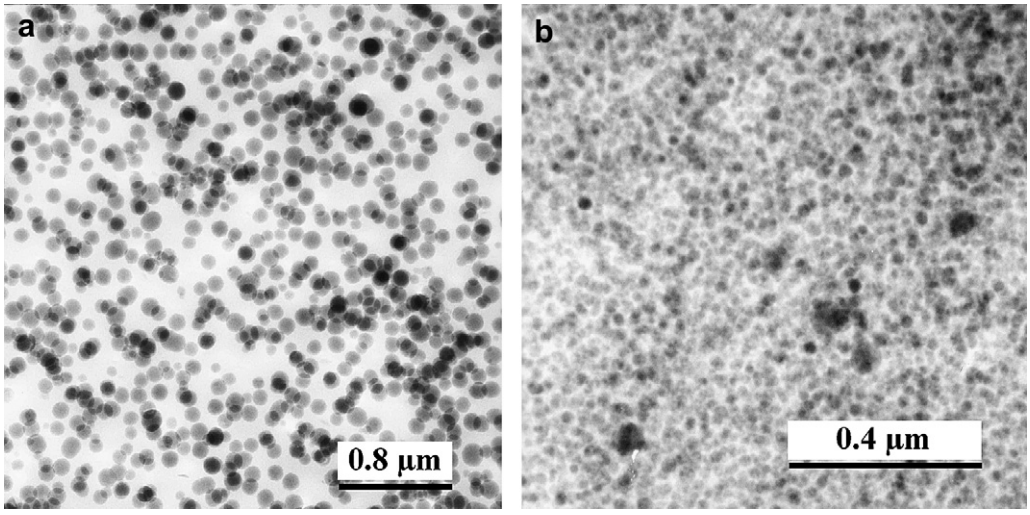

Fig. 2. TEM micrographs for particle-dispersion investigation in high NS content (17.4 vol %): (a) 80ESN, (b) 20ESN.

each formulation were tested. The fracture energy, G_{IC}, was calculated using Equation (1) [18]. Where E is Young's modulus, which was estimated from compression test results. The Poisson's ratio, ν, is taken as 0.39 for this epoxy system [19].

$$G_{IC} = \frac{K_{IC}^2}{E}\left(1-\nu^2\right) \tag{1}$$

The number average molecular weight between crosslinks of neat epoxy, i.e. M_c value, can be calculated from a variety of methods [3]. In this study, Equation (2), which is based on the theory of rubber elasticity [20], was applied. Where q is the front factor (assumed as 1 in this work); T is the temperature (K); ρ is the density of the matrix at temperature T; R is the universal gas constant, and G_r is the equilibrium shear modulus in the rubbery region at temperature T.

$$M_C = \frac{q\rho RT}{G_r} \tag{2}$$

The density of the neat epoxy at elevated temperatures was estimated using the coefficient of thermal expansion (CTE). The linear CTEs for the three neat epoxy resins were measured using a thermal mechanical analyzer (TMA, model 2940, TA Instrument) with heating rate of 1 °C/min.

The relaxed shear modulus, G_r, was measured using an advanced rheometric expansion system (ARES, Rheometric Scientific). Sample dimensions were nominally 65 mm × 12.7 mm × 3.2 mm. G_r, was taken at $T_g + 50$ °C, where the T_g values were determined by the data from DSC. The testing vibration frequency was kept at 1 Hz; strain amplitude was 0.2%, and the temperature was increased using 5 °C steps with 5 min dwell time.

Scanning electron microscopy (SEM, model 4300, Hitachi) was applied to study the fracture surfaces. Before the SEM investigation, the fractured surfaces from the 3PB specimens were coated with Iridium as the electrically conductive layer through sputter coating (turbo sputter coater, model EMS575X, Electron Microscopy Sciences). The coating condition was chosen as following to maintain the 5 nm thick Iridium layer: coating current 20 mA, coating time 30 s, and operating pressure 5×10^{-1} mbar. During the SEM examination, the accelerating voltage was kept under 5 kV to prevent beam damage to the surfaces.

In order to investigate the subsurface damage, thin sections at the mid-plane that are perpendicular to the fracture surfaces are obtained from fractured 3PB specimens. Before analyzing the thin sections under the transmitted light optical microscopy (TOM,

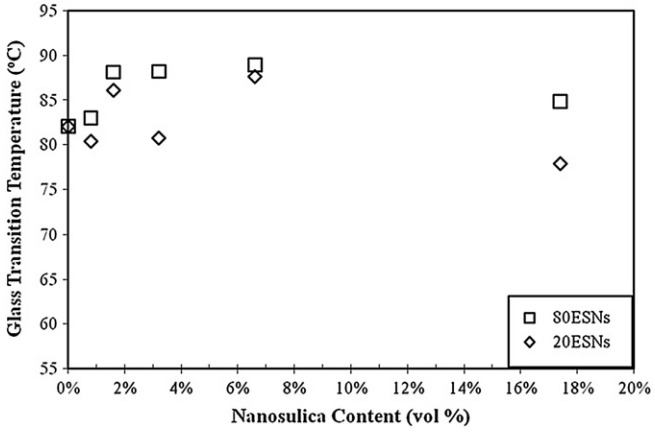

Fig. 3. The T_g values of ESNs plotted versus the NS fraction.

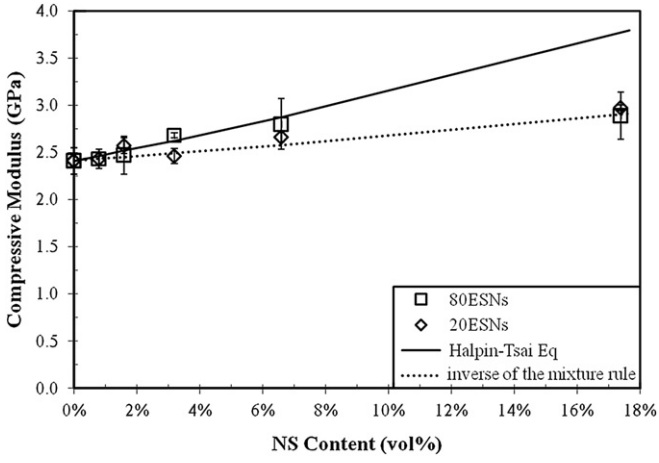

Fig. 4. Compressive moduli versus NS content. Hollow symbols are the experimental results. The solid line represents Halpin-Tsai model, and the dot line represents the simple series.

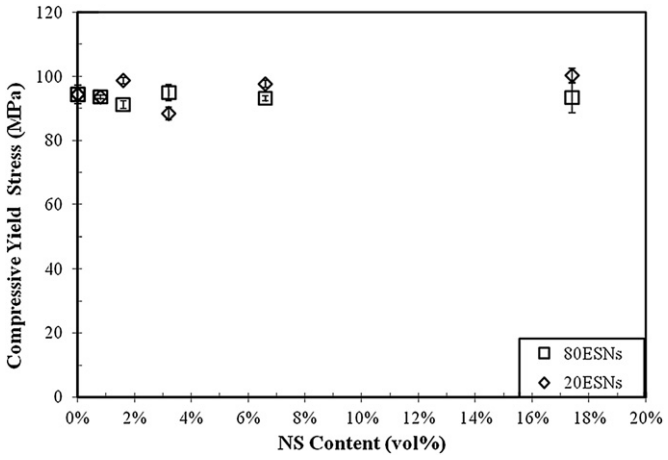

Fig. 5. The compressive yield stress of ESNs obtained under room temperature.

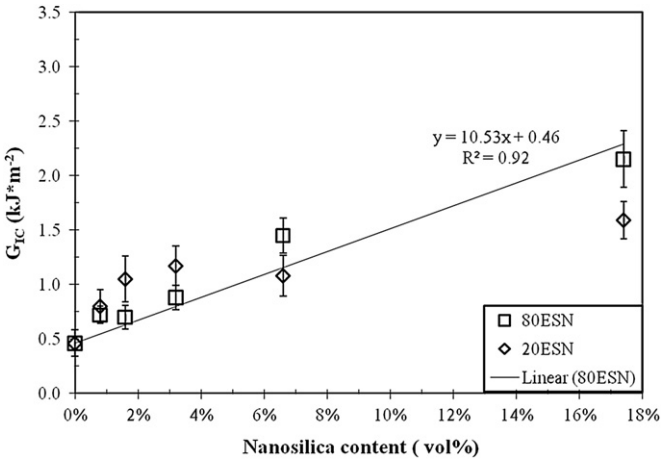

Fig. 7. The fracture energy of ESNs varies with NS content.

model BH2, Olympus), these thin sections were ground and polished using standard petrographic techniques [21] to 80–120 μm in thickness. The thin sections were examined under both bright field and cross polars.

3. Results and discussion

3.1. NS particle dispersion

The TEM images in Figs. 1 and 2 show the NS-particle distribution in ESNs. Randomly dispersed NS particles are shown and agglomerated particles are not observed at low NS content for both 80 ESN (with 80 nm NS particles) and 20 ESN (with 20 nm NS particles). At high NS content, a small amount particle clustering can be observed (see Fig. 2). Similar random dispersions have been observed in other nanosilica-filled epoxy studies [8–12].

3.2. Thermal properties of ESNs and neat epoxy resins

The T_g values measured using DSC are plotted vs. the NS content in Fig. 3. The T_g of neat epoxy resin (DGEBA/piperidine, cured at 160 °C) is 82 °C, which is in agreement with the results in Pearson and Yee's work [22]. The T_g values of both 20 ESNs and 80 ESNs are scattered around 82 °C within a range of ±6 °C. Similar scatter in T_g values can be found in other ESNs studies [12,23]. Therefore, the addition of NS particles does not change the polymer chain mobility of the bulk materials for this DGEBA/piperidine epoxy system.

3.3. Compressive modulus and compressive yield stress

The compressive moduli of ESNs were obtained from the linear portion of the stress–strain curves in compression tests, where the strain range was usually between 2% and 4%. The results are shown in Fig. 4, and the error bar is the standard deviation for more than 5 measured values. The compressive moduli of ESNs moderately increase with the amounts of NS content, and the relative improvement in compressive modulus, ($E_{ESN}/E_{neat\ resin}$), reaches 1.2 when NS content is 17.4 vol%. This trend in modulus coincides with the results reported by Zhang et al. [9] and Johnsen et al. [12]. Both Zhang and Johnsen demonstrated the highest relative improvement of Young's modulus in ESNs is around 1.3 when the highest NS content, approximately 14 vol%, is used.

Two quantitative models, Halpin–Tsai and simple series, are applied in Fig. 4. Halpin–Tsai [24,25] model, which is a common option to predict the increase of Young's moduli in filled polymer composites, is shown in Equation (3). Where E_c, E_m, E_f are Young's modulus of the composite, the polymer matrix, and the filler respectively; V_f is the volume fraction of the filler, and ξ is the shape factor of the filler, which is defined as the length of the filler divided

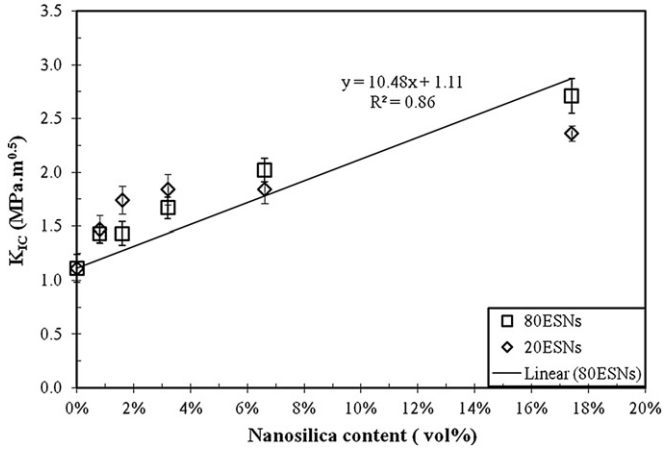

Fig. 6. The fracture toughness of ESNs varies with NS content.

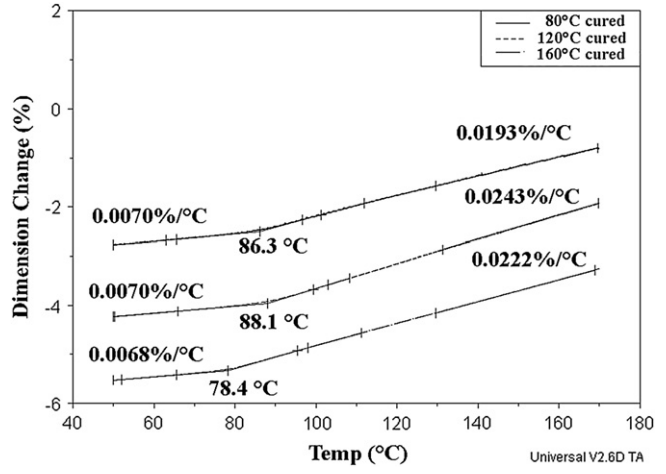

Fig. 8. Dimension change due to the thermal expansion of neat epoxy resins.

Table 2
The densities changed due to thermal expansion for neat epoxy resins.

Cure Schedule	T_g from TMA (°C)	Linear CTE below T_g (ppm/°C)	Linear CTE above T_g (ppm/°C)	Volume expansion ($V_{Tg+50\,°C}/V_{25\,°C}$, %)	ρ at 25 °C (g/cm^3)	ρ at T_g+50 °C (g/cm^3)
80 °C for 24 h	86.3	70	193	104.3%	1.18	1.13
120 °C for 16 h	88.1	70	243	105.0%	1.18	1.12
160 °C for 6 h	78.4	68	222	104.6%	1.18	1.13

by its thickness and multiplied by two. ξ equals 2 since the filler shape is spherical. The simple series model, which is also known as the inverse of the mixture rule, assumes the equal stress state between the fillers and the matrix under the loading [26] (see Equation (4)).

$$E_c = \frac{1+\xi\eta V_f}{1-\eta V_f}E_m \quad \eta = \frac{\left(\frac{E_f}{E_m}-1\right)}{\left(\frac{E_f}{E_m}+\xi\right)} \tag{3}$$

$$E_c = \left(\frac{(1-V_f)}{E_m}+\frac{V_f}{E_f}\right)^{-1} \tag{4}$$

By applying Young's modulus of bulk silica as 70 GPa [27], and the neat epoxy resin as 2.41 GPa, the prediction results of Halpin–Tsai model and simple series model are plotted as the solid line and dotted line, respectively in Fig. 4. Both models adequately describe the enhancement of compressive moduli in ESNs, although Halpin–Tsai model slightly overestimates the enhancement when the NS volume fraction is beyond 6.6 vol%. Interestingly, Halpin–Tsai model also demonstrated a similar overestimation trend in the ESN study reported by Johnsen et al. [12].

It is noteworthy that no significant difference in modulus between 20 ESNs and 80 ESNs is observed in Fig. 4. Indeed, there are different opinions about the particle size effect on Young's modulus of rigid sphere filled, glassy polymer composites in the literature. On the one hand, some studies demonstrated a particle size effect on Young's modulus of the composites is more significant for nanometer size spheres. For example, in a poly(vinyl ester) composite system, which is reinforced by 1–3 h vol% alumina particles, Cho et al. [28] reported that Young's moduli of the composites increase when the size of particles decreases to the nanometer range. Zhang et al. [9] also demonstrated the relative improvement of Young's modulus in ESNs is more considerable when the interparticle distance (τ) is smaller than the particle diameter (d). On the other hand, other studies have shown that Young's moduli of the polymer composites filled with micron size spheres are mainly a function of the filler volume fraction, Young's moduli of the filler and polymer matrix, but not the size of the filler [27,29,30]. The reasonable agreements between the prediction models and the experimental data shown in Fig. 4 imply the compressive modulus of ESNs is mainly a function of the NS content and not the NS particle size. In addition, no extra relative improvement in the high NS content region (17.4 vol%, where $\tau/d < 1$) is observed in these particular ESNs systems.

The compressive yield stresses of ESNs are shown in Fig. 5. The values of yield stress from ESNs are independent on the NS fraction. Zhang et al. [9] also reported that the yield stress of ESNs obtained from the tensile test does not increase with the NS content. Nevertheless, this observation is somewhat unexpected since Kawaguchi and Pearson [31] and Amdouni et al. [32] have demonstrated that the compressive yield stress of the composite increases with filler content for the micron glass beads filled epoxy systems. Obviously, more research is needed to understand the discrepancy of compressive yield stress in ESNs and the epoxies toughened by micron glass beads.

3.4. The effect of particle size on fracture behavior

The K_{IC} values of ESNs are shown in Fig. 6. The error bar is the standard deviation for at least 5 measured values. These results reveal that the improvement of fracture toughness scales linearly with NS content. The G_{IC} values of ESNs (see Fig. 7) also improve with NS content. The above observations are in agreement with other ESNs studies [8–12]. Two facts related to the K_{IC} values are noteworthy. First, the K_{IC} of 80 ESN reaches 2.71 MPa m$^{0.5}$, when NS loading is 17.4 vol%, which is the highest K_{IC} value from epoxy–silica

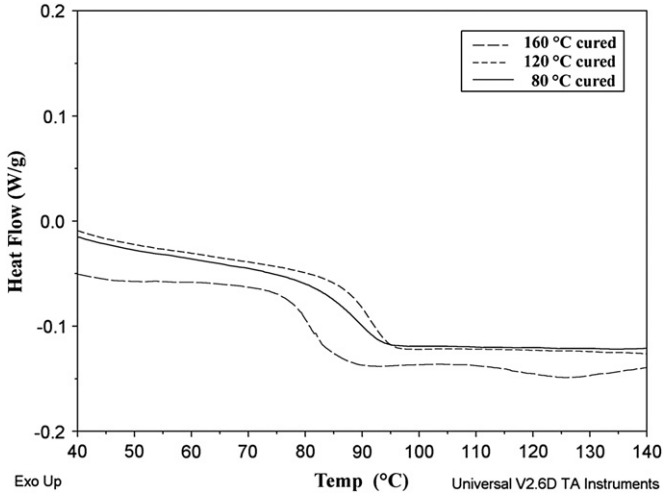

Fig. 9. The experimental data of T_g from the neat epoxy resins under different curing schedules.

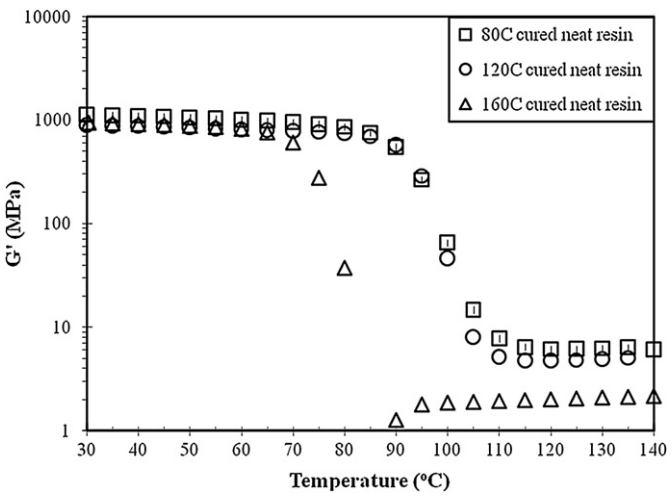

Fig. 10. The experimental data of G_r from the neat epoxy resins under different curing schedules.

Table 3
M_c and the relative improvements of K_{IC} and G_{IC} under different curing schedules.

Cure Schedule	T_g (°C)	G_r (MPa)	ρ at $T_g + 50$ °C (g/cm^3)	M_c (g/mol)	$K_{IC\ (ESN)}$ (MPa*m$^{0.5}$)	$K_{IC\ (neat\ epoxy)}$ (MPa*m$^{0.5}$)	$K_{IC\ (ESN)}$/ $K_{IC\ (neat\ epoxy)}$	$G_{IC\ (ESN)}$/ $G_{IC\ (neat\ epoxy)}$
80 °C for 24 h	89.8	9.50	1.13	359	1.13	0.67	1.64	2.25
120 °C for 16 h	91.3	5.91	1.12	574	1.56	0.84	1.82	2.76
160 °C for 6 h	82.0	2.17	1.13	1536	2.36	1.11	2.13	3.61

nanocomposites reported in open literature to date [8–12]. Second, although our experimental results (fracture toughness and fracture energy) demonstrate that the difference between 20 ESNs and 80 ESNs is negligible after taking the standard deviation into account, it appears that the NS particles are more efficient in toughening epoxies than micron size glass spheres. A fairly comparative benchmark would be Kawaguchi and Pearson's work [33]. They studied the fracture toughness of the epoxies toughened by micron size glass spheres (mean diameter 42 μm) in a very similar matrix system (DGEBA/piperidine, cured at 160 °C). The K_{IC} values of micron size glass bead-filled epoxies also scales with filler content. More importantly, K_{IC} values of 2.5 MPa m$^{0.5}$ can be achieved, but such toughness was only achieved when twice the filler content were used (30 vol%).

In micron size, glass sphere filled epoxy systems, some studies [2,33] have shown the influence of particle-matrix interface on toughening behavior is negligible when the specimens were tested dry as molded. However, the importance of particle-matrix interface in ESNs cannot be neglected since the interface area dramatically increases due to the tininess of nanosilica. A comparable example can be found in the recent study reported by Zhao et al. [34]. They have demonstrated that a stronger interface is beneficial to the fracture energy in a nanoscale alumina filled epoxy. Although the 20 nm NS particles and 80 nm NS particles came from different sources in the present study, it is assumed that both particle-surface treatments are similar. As a result, the difference of particle-matrix interface between 20 nm NS and 80 nm NS is insignificant. In fact, another investigation using different sizes NS particles with the same surface treatment is ongoing in our group, and the preliminary results also indicate the NS particle size effect on toughening behavior is not significant in the similar particle-size range.

3.5. The effect of matrix crosslink density

Crosslink density is often measured in terms of the number of crosslinks per unit volume or the number average molecular weight between crosslinks, M_c. The importance of epoxy matrix crosslink density on fracture toughness was first emphasized in rubber toughened epoxy resins [35,36]. For example, Pearson and Yee [35] used several DGEBA epoxides with varied epoxide equivalent weights to control the crosslink density for 4,4′-diamino diphenyl sulphone (DDS) cured epoxy systems. Rubber particles show much more efficiency in toughening the epoxies with lower matrix crosslink density. The epoxy resins with lower crosslink density are more ductile, hence the materials endure more plastic shear deformation and dissipate more strain energy [35,36]. A study by Lee and Yee [3] reported that the epoxy matrix toughened by rigid glass spheres has a similar dependence on the crosslink density. For example, with the same amounts of micron glass spheres, the relative improvement of fracture toughness ($K_{IC\ (composite)}/K_{IC\ (neat\ epoxy)}$) scales up from 1.40 to 1.98 when the M_c increases to 12.3 fold of its original value [3].

In many epoxy systems the crosslink density can be controlled by manipulating the epoxide equivalent weight, however, for the

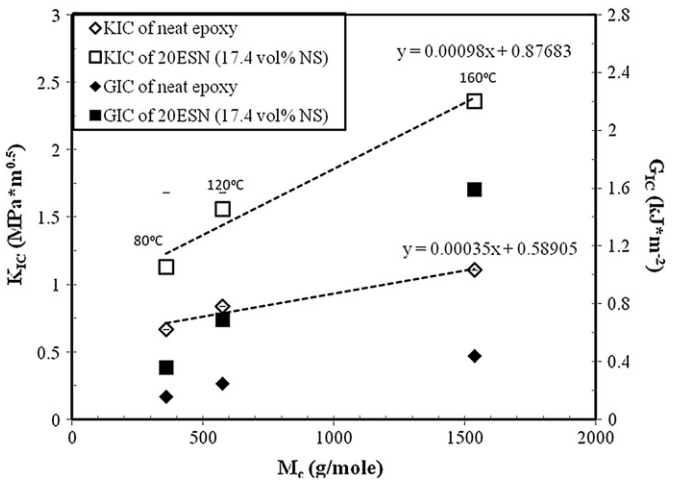

Fig. 11. The effect of M_c values on the fracture behavior.

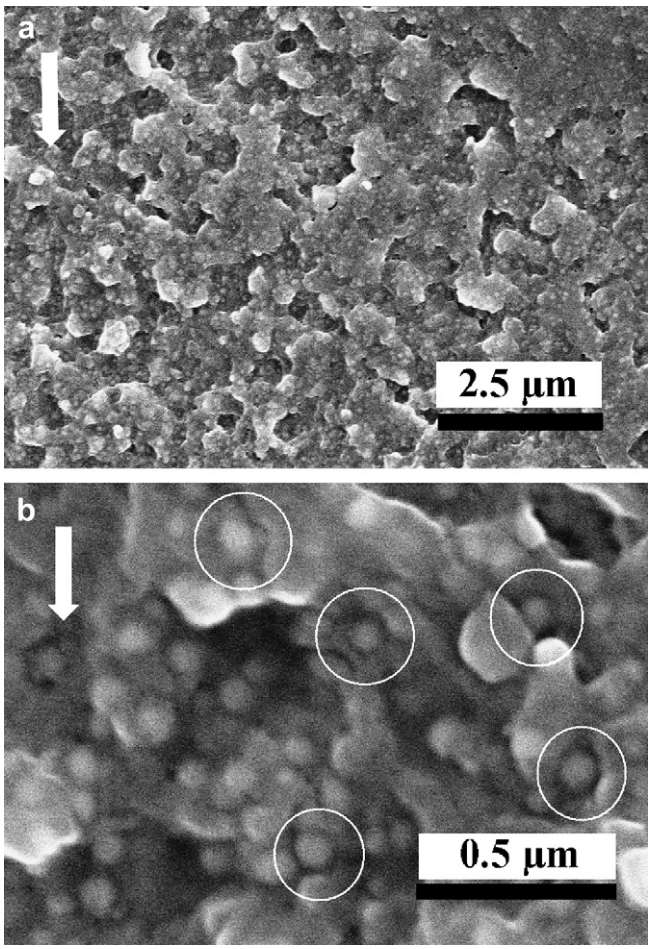

Fig. 12. SEM micrographs from 17.4% 80ESN fracture surface: (a) the wave pattern demonstrates the matrix-ligament bridging, (b) debonded particles are emphasized in white circles under higher magnification.

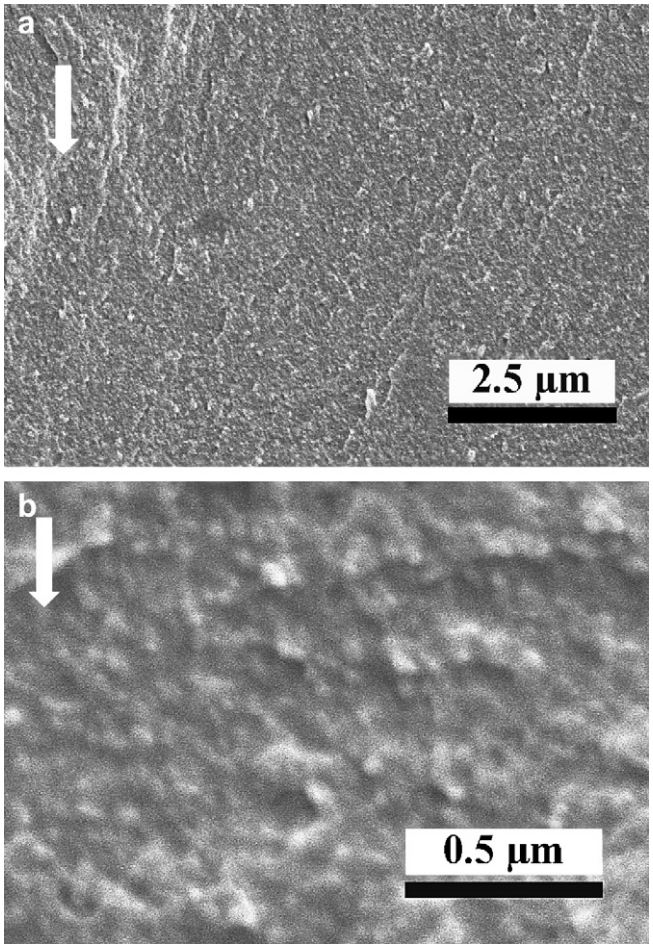

Fig. 13. SEM micrographs from 17.4% 20ESN fracture surface: (a) smooth fracture surface (b) higher magnified view.

piperidine cured epoxy system the crosslink density can also be controlled by changing the cure temperature. Kinloch et al. [36] showed the M_c in a DGEBA/piperidine system can be increased to 8.3-fold by changing the curing conditions from 120 °C to 160 °C. To demonstrate the effect of epoxy-crosslink density on the fracture toughness of ESNs, three curing conditions are chosen here. They are 80 °C for 24 h, 120 °C for 16 h, and 160 °C for 6 h.

As mentioned in the experimental approach (see Equation (2)), one needs both the density and the relaxation modulus at $T_g + 50$ °C to calculate the average molecular weight between crosslinks in epoxy systems. The density at $T_g + 50$ °C can be calculated using CTE measurements and the density at room temperature. The dimensional changes due to the thermal expansion of the neat epoxy resins are plotted vs. temperature in Fig. 8. The parallel curves obtained from different neat epoxy resins reveal their thermal expansion coefficients (ppm/°C) are similar. Using the linear expansion measured from TMA, the volumetric expansion of neat epoxy resins can be determined (see Table 2). At $T_g + 50$ °C, the volume of all three neat epoxy resins expanded by 4–5% of their original volume at room temperature. Thermal expansion results in a slight decline of the epoxy-resin density from 1.18 g/cm^3 (at room temperature, [36]) to a range between 1.13 and 1.12 g/cm^3 (at $T_g + 50$ °C). In other words, any density differences between the neat epoxy resins cured under the three different curing schedules are trivial.

The experimental data in T_g (measured by DSC) and the G_r at $T_g + 50$ °C (measured by ARES) of neat epoxy resins are shown in Figs. 9 and 10, respectively. Table 3 includes the T_g values, the G_r values, the M_c values (calculated from Equation (2)), the relative improvements of fracture toughness ($K_{IC\ (composite)}/K_{IC\ (neat\ epoxy)}$) and fracture energy ($G_{IC\ (composite)}/G_{IC\ (neat\ epoxy)}$) from 20 ESNs (17.4 vol% NS). For the fracture energy calculation shown here, please note that Young's moduli of the neat epoxies and ESNs cured under 120 °C and 80 °C are assumed the same as the counterparts cured under 160 °C. This assumption is reasonable since the results in Fig. 10 indicate no significant difference of the shear modulus obtained under room temperature between these three curing schedules.

The results in Fig. 11 demonstrate that the K_{IC} and G_{IC} values of 20 ESNs have more M_c dependence compared with neat resin. Moreover, the decreased toughening efficiency in the 20 ESNs is due to the lower M_c values (or higher matrix crosslink density), which is controlled by curing conditions. This observation is in agreement with the literature [3,35]. Though the M_c values of the neat epoxy cured at 80 °C and 120 °C shown in this study are similar to Pearson's work [19], the M_c value of the neat epoxy cured at 160 °C is lower than the results reported by other researchers. For example, Pearson and Kinloch et al. [35,36] estimated the M_c value of 160 °C cured DGEBA/piperidine is 5002 and 4900 g/mol, respectively.

3.6. Fracture surface of ESNs

The 80 ESN fracture surfaces near the precrack front region were examined under SEM. The white arrows at the top left corners in Fig. 12 indicate the crack growth direction. Matrix–ligament bridging is observed in Fig. 12(a) and debonded particles are seen under higher magnification in Fig. 12(b). Matrix–particle debonding is essential in the matrix plastic void growth mechanism, which is a significant part of the matrix plastic deformation in ESNs [12].

In contrast to Fig. 12, the fracture surface of 20 ESN is remarkably smooth (see Fig. 13). The smaller, 20 nm NS particles are hard to detect even at higher magnification (Fig. 13(b)) since the particle size and the thickness of conductive coating layer (around 5 nm) is the same order of magnitude. In addition, bowing lines and tails behind particles on the fracture surface are not seen in both 80 ESN and 20 ESN to support the crack pinning mechanism.

A physical limitation of applying the crack pinning model to ESNs has also been discussed in the literature [12]. Since the crack pinning concept is developed by the concept that impermeable particles locally pin the crack front and result in tension-line bowing, the particles should be bigger or at least equal to the crack opening displacement (COD). Based on the above concept, Johnsen et al. [12] calculated the size of COD using Irwin's analysis for the line zone ahead of the crack tip under plane strain conditions as in Equation (5) [37].

$$\delta_{tc} = \frac{K_{IC}^2}{E\sigma_y}\left(1-\nu^2\right) = \frac{G_{IC}}{\sigma_y} \tag{5}$$

where σ_y is the yield stress and ν is the Poisson ratio. The comparison of the calculation results and the TEM images showed a tremendous difference between COD and NS particle sizes (4.7 μm and 20 nm, respectively). It is unambiguous that NS particles are too small to pin the crack front. The same size-difference elucidation is also applied to interpret the mismatch of crack deflection concept in ESN system [12].

3.7. Subsurface damage

In order to analyze the nature of the subsurface damage, our observations focused on the slow crack growth region located near

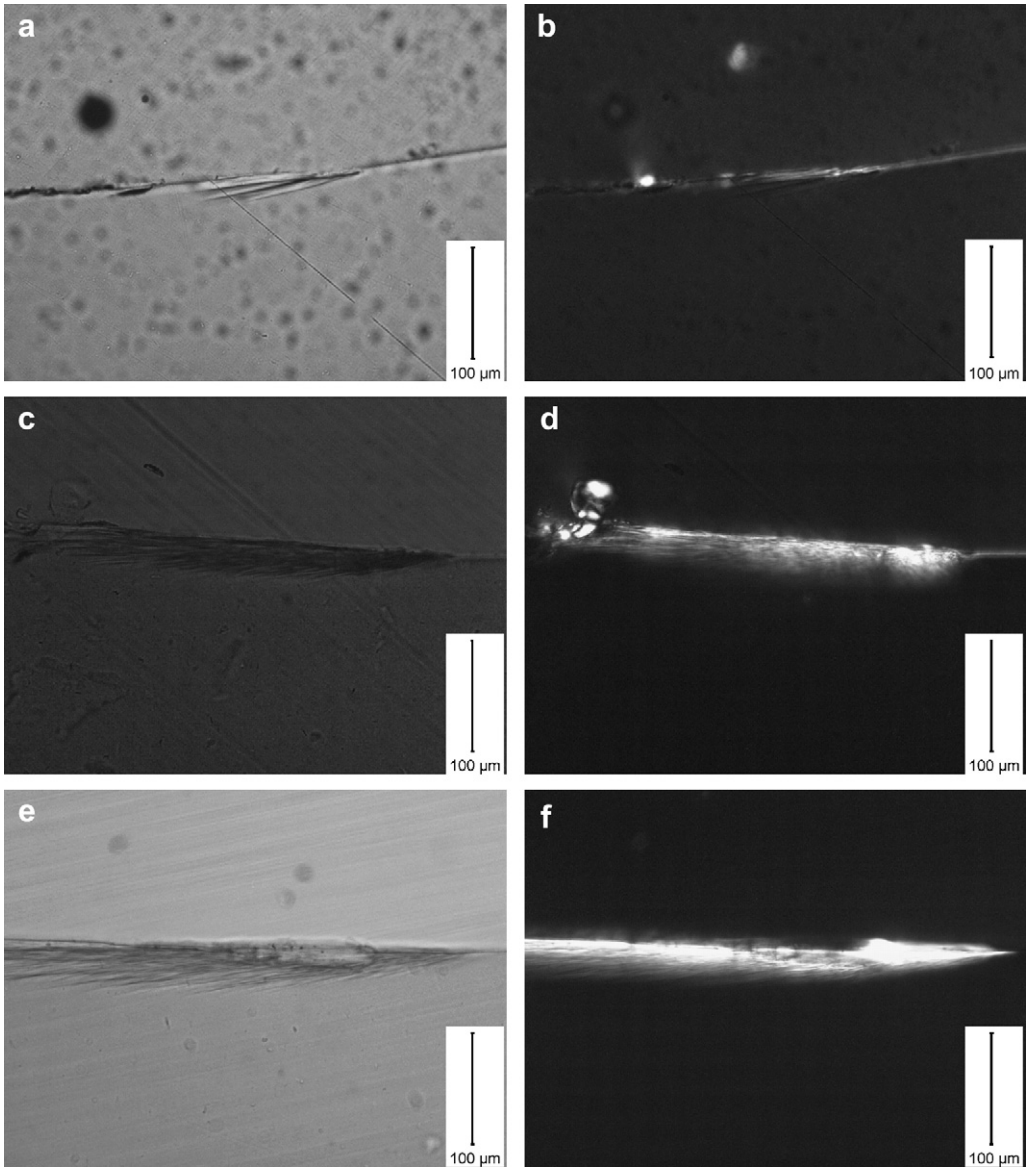

Fig. 14. The TOM micrographs of 80ESNs (a) 1.6 vol% NS under bright field; (b) under cross polars; (c) 6.6 vol% NS under bright field; (d) under cross polars; (e) 17.4 vol% NS under bright field, and (f) under cross polars. The crack growth direction is horizontally from right to left. Note size of matrix dilation bands scales up with NS content.

the precrack tip from the 80 ESNs. The TOM micrographs in Fig. 14 were taken under bright field or under cross polars. The crack growth direction is from right to left. The horizontal lines cutting through the mid-part of every picture are the fracture surfaces, and the subsurface regions are represented by the bottom halves. A comparison of plastic zone size as a function of 80 nm-diameter NS content is presented by 80 ESNs with 1.6 vol%, 6.6 vol%, and 17.4 vol% NS. Under bright field, dark bands are observed below the fracture surface in 6.6 vol% and 17.4 vol% NS specimens (see Fig. 14(c) and (e), respectively). In contrast, only several dark lines present in 1.6 vol% NS specimen (see Fig. 14(a)). Under cross polars (see Fig. 14(b), (d), and (f)), bright birefringent regions under the fracture surfaces of ESNs are seen due to the orientation of the epoxy. In fact, birefringence is usually used to detect shear bands [38–43]. It is important to note that the size of the dark-band/shear banding regions scales up with the NS contents as well as the K_{IC} values.

Though massive shear banding was first used to explain the toughening for rubber modified epoxies [38,39], the existence of shear banding in micron glass bead filled epoxies has attracted more attention recently. Lee and Yee [40,41] proposed that "microshear banding" is one of the main toughening mechanisms in glass bead filled epoxies. Kawaguchi and Pearson [31,33,42,43] confirmed the presence of microshear banding in micron glass sphere filled epoxies using optical microscopy on the sections taken from compression tests, however, the features of these bands were notably different than those observed at the crack tip.

Kawaguchi and Pearson attributed that the dark bands at crack tips to microcracks in their studies. Since pure shear banding should not be seen under bright field, and microcracking usually disappears under cross polars, the dark bands shown in Fig. 14(a), (c) and (e) are more complex. In fact, those dark bands are presumed to be the dilatational bands for the following reasons. Lazzeri and Bucknall [44] indicated that the dilatational bands form when both shear yielding and the volume dilation normal to the shear plane are presented. Literature supports the occurrence of the matrix dilation in ESNs. For example, by carefully examining the results of SEM and atomic force microscopy, Johnsen et al. [12] demonstrated that the matrix dilation occurs around the debonded

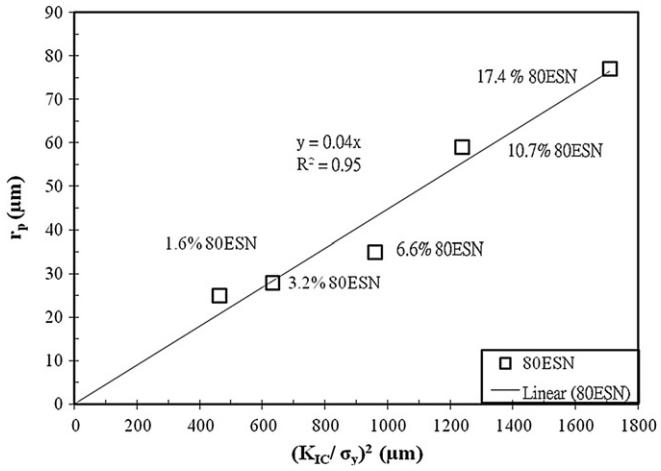

Fig. 15. Measured plastic zone size versus $(K_{IC}/\sigma_y)^2$.

NS particles. Furthermore, debonded NS particles are also seen in this study (see Fig. 12). Another strong evidence is the overlapping between the dark-band regions and the shear banding regions (see Fig. 14), which reveals the dark bands are coupled with the shear banding. This observation is somewhat in agreement with the study reported by Speroni et al. [45] and Pearson and Yee [39], which indicated that the extensive cavitation, i.e. matrix dilation, is preferentially associated with shear banding in the rubber toughened polyamide system, and the rubber toughened epoxy system, respectively.

Combining the results in fracture surface and subsurface damage shown above, one may conclude that the debonding between matrix–NS particle reduces the triaxiality in the ESNs and leads to plastic deformations, i.e. void growth and shear banding. It appears as the plastically deformed, birefringent regions shown in Fig. 14 belong to a crack tip zone shielding mechanism. Ideally, the process zone blunts the subsequent crack front and the size of the process zone scales with the fracture behavior of the material. In order to evaluate this process zone concept, the depths of the plastic deformations are measured in 80 ESNs and compared with theoretical predictions. According to Irwin's model [46], the radius of the plastic zone, r_p, which equals the depth of the plastic zones in 3PB specimens, can be expressed as Equation (6) for plane strain conditions. Where σ_y is the yield stress, which is the experimental data from compressive test multiplied by 0.7 according to ASTM D5045 guideline [18]. The values of plastic zone depth measured from 80 ESNs, r_p, are plotted vs. the parameter derived from Irwin's predictions, $(K_{IC}/\sigma_y)^2$, in Fig. 15. It shows that the values of r_p have a strong linear dependence on $(K_{IC}/\sigma_y)^2$.

$$r_p = \frac{K_{IC}^2}{(6\pi)\sigma_y^2} \tag{6}$$

Since the σ_y values of ESNs can be treated as a constant according to Fig. 7, one may conclude that the increase of fracture toughness would be mainly due to the increase of plastic zone size by Irwin's prediction. In addition, the slope of the linear regression is calculated as 0.045, which is close to the value from Irwin's model $(1/6\pi)$, 0.053. The agreement between the plastic zone size measurements and the predictions from Irwin's model further corroborates our hypothesis that plastic deformation at the crack-tip is the major toughening mechanism in these ESNs.

Table 4
The properties of the materials used in Equation (7).

μ_m	σ_{yc}	γ_f	r_{yu}	K_{vm}	NS diameter	Void diameter
0.2 [48]	[a]94.4 MPa	0.71 [48]	[a]15 μm	2.22 [47]	[a]80 nm [a]20 nm	[a]118 nm [a]29.6 nm

[a] In the present study.

Table 5
The predicted ΔG_v from results reported by Johnsen et al. [12].

Nanosilica (vol%)	ΔG_v ((kJ/m^2) our calculations	ΔG_v (kJ/m^2) from [12]
2.5	105	107
4.9	206	209
7.1	299	297
9.6	404	394
13.4	564	540

3.8. Modeling fracture toughness in ESNs

In contrast to the plastic void growth model applied by Johnsen et al. [12], the TOM observations in Fig. 14 reveal that the plastic deformation consists of matrix dilation bands as well as matrix shear bands. Thus the quantitative prediction of fracture energy in ESNs should include the contribution from shear banding. Actually, the original model used in Johnsen's work, which was proposed by Huang and Kinloch [47,48] to predict the improvements in fracture energy for rubber toughened epoxies, contained the shear banding and the plastic void terms (see Equation (7)) as well as a term for rubber particle stretching (not shown).

$$G_{IC}^{ESN} = G_{IC}^{Neat} + \Psi$$

$$\Psi = \Delta G_s + \Delta G_v$$
$$\Psi = 0.5 \times \left(1+\mu_m/3^{1/2}\right)^2 \times \left[\left(4\pi/3V_f\right)^{1/3} - 54/35\right] \times V_f \sigma_{yc} \gamma_f r_{yu} K_{vm}^2 + \left(1-\left(\mu_m^2\right)/3\right) \times \left(V_{fv} - V_{fr}\right) \times \sigma_{yc} r_{yu} K_{vm}^2 \tag{7}$$

where Ψ is the overall toughening contribution; ΔG_s and ΔG_v are the contributions from localized shear banding and plastic void growth, respectively; μ_m is a material constant (pressure coefficient); V_{fr} and V_{fv} are the volume fraction of initial rubber particles, and voids, respectively. Since Equation (7) is applied for ESN systems here, V_{fr} is equivalent to V_{fp}, which means the volume fraction of initial NS particles. σ_{yc} is the compressive yield stress of the epoxy matrix; γ_f is the shear fracture strain of the epoxy matrix; r_{yu} is the radius of plastic zone in unmodified epoxy, and K_{vm} is the maximum stress concentration factor of the von Mises stress in the epoxy matrix. In this study, σ_{yc} was found to be 94.4 MPa, and r_{yu} is calculated to be 15 μm using Equation (6). Since the experimental materials in this study are similar to Kinloch and Huang's work [48] (DGEBA/piperidine, cured at 160 °C), the pressure coefficient, μ_m, and the shear fracture strain of the epoxy matrix, γ_f, are taken as the same numbers in Ref. [48], which are 0.2 and 0.71, respectively. According to the finite-element analysis in Ref. [47], the value of K_{vm} around a void in epoxy matrix is 2.22, which was also used in Johnsen's work [12]. In order to obtain $(V_{fv} - V_{fp})$, the size of voids is estimated from the SEM micrograph. The average diameter of voids is 118 nm (based on the five clearest voids circled in Fig. 12). The ratio of the diameter of voids to the diameter of particles ($D_{voids}/D_{particles}$) is 1.48, which is close to the results reported by Johnsen et al. [12]. They measured the size of voids using AFM and reported the average diameter of voids is 30 nm for an epoxy filled with 20 nm-diameter NS particles. All NS particles were assumed to be debonded. The values mentioned above are shown in Table 4.

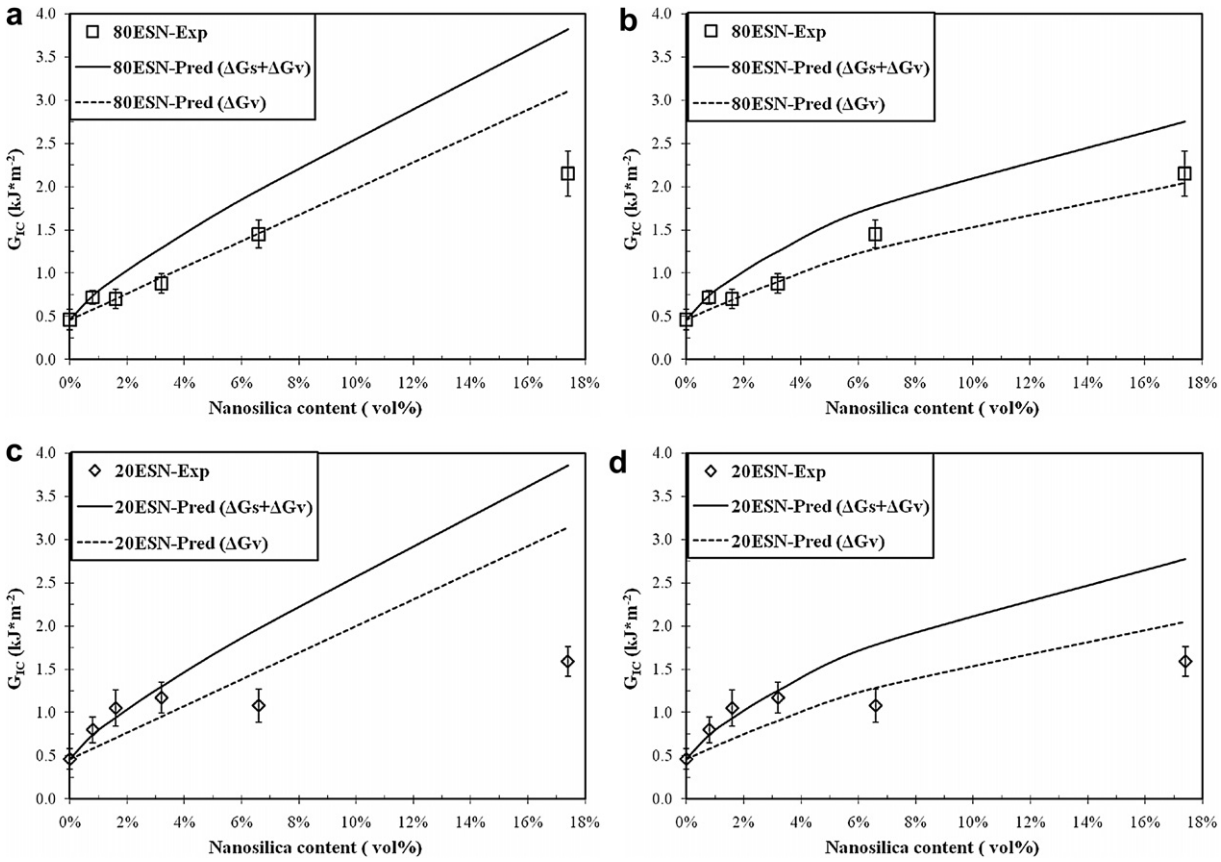

Fig. 16. The experimental data and predicted values according to Eq. 7; (a) and (c) use Eq. 10 to calculate void growth; (b) and (d) use Eq. 12 to calculate void growth.

The calculation of increased volume fraction of voids, $(V_{fv} - V_{fp})$, is essential for determining ΔG_v in Equation (7). Huang and Kinloch [48] assumed that

$$\frac{V_1}{V_o} = \frac{V_{fv}}{V_{fr}} \tag{8}$$

where V_o and V_1 are the volume of materials before and after deformation (plastic dilation), respectively. Since the volume fraction of voids is difficult to measure in nanosilica filled epoxies Johnsen et al. [12] used an average particle size and an average void size to determine the volume fraction of voids. Although not explicitly described by Johnsen et al. [12], we repeated their calculations assuming:

$$\frac{V_{fv}}{V_{fp}} = \frac{v_v}{v_p} \tag{9}$$

where v_v and v_p is the average volume of voids and NS particles, respectively. Hence, $(V_{fv} - V_{fp})$ can be expressed as Equation (10).

$$\left(V_{fv} - V_{fp}\right) = \left(\frac{v_v}{v_p} - 1\right) \times V_{fp} \tag{10}$$

The predicted ΔG_v values from our calculations are shown in Table 5. Note that 29.6 nm is used as the average void diameter in our calculations. These results show a reasonable agreement with the predicted values reported by Johnsen et al. [12], who stated an average void diameter is 30 nm was used.

Interestingly, if the volume of matrix is expressed as v_m, and V_{fp} in Equation (9) is substituted for $v_p/(v_m+v_p)$, Equation (9) becomes

$$V_{fv} = \frac{v_v}{v_m + v_p} \tag{11}$$

Equation (11) reveals the inaccuracy of Equation (9). Therefore, another approach of estimating $(V_{fv}-V_{fp})$ is proposed here. The volume of matrix around the NS particle, v_m, is calculated as: $v_m = v_p/V_{fp} - v_p$. v_m is kept constant before and after voiding. By doing so, $(V_{fv} - V_{fp})$ can be expressed as Equation (12):

$$\left(V_{fv} - V_{fp}\right) = \left(\frac{v_v}{v_v + v_m} - \frac{v_p}{v_p + v_m}\right) \tag{12}$$

The predicted and measured G_{IC} values of ESNs are plotted in Fig. 16. Please note that the model combining shear banding and plastic void growth $(\Delta G_s + \Delta G_v)$ is shown as the solid line while the plastic void growth model (ΔG_v) is shown as the dotted line. Fig. 16(a) and (c) contains the predicted G_{IC} values by using Equations (7) and (10) for 80 ESNs and 20 ESNs, respectively. Alternatively, Fig. 16(b) and (d) shows the predicted G_{IC} values using Equations (7) and (12).

As shown in Fig. 16(a) and (c), ΔG_v (dotted line) demonstrates a linear relationship with NS content for 80 ESNs and 20 ESNs, respectively. Compared with experimental data, considerable overestimation of predicted G_{IC} values is seen in these cases, especially when NS content reaches 17.4 vol%. Such overestimations were also reported the study reported by Johnsen et al. [12], and they mainly attributed this deviation to the simplifying assumption that all NS particles debond and initiate plastic void growth. Indeed, our fracture surface study agrees with this explanation hence the SEM micrographs shown in Fig. 12 reveal that particle–matrix bonding remains intact in many cases. However, the overestimations seen in Fig. 16(a) and (c) can also be significantly improved when Equation (10) were substituted by Equation (12). The ΔG_v model closely matches the experimental results

obtained from 80 ESNs in Fig. 16(b), although the experimental data from 20 ESNs are still slightly lower than values predicted by the ΔG_v model (see Fig. 16(d)).

In brief, the plastic void growth (ΔG_v) model, which was proposed by Johnsen et al. [12], provided essential ideas to understand the toughening mechanism in ESNs in microcosm. In this model, determining the increased volume fraction of voids, $(V_{fv} - V_{fp})$, is critical. Equation (12), which emphasizes the concept that the matrix does not shrink after voids, is notably helpful to diminish the overestimation in $(V_{fv} - V_{fp})$ and increases the accuracy in fracture-energy prediction. However, the ΔG_v model neglects the influence of shear banding in toughening mechanism, therefore, an attempt of combining shear banding and plastic void growth $(\Delta G_s + \Delta G_v)$ in modeling fracture energy of ESNs is presented above. The model used in this study originally came from Huang and Kinloch's studies [47,48]. Unfortunately, the $(\Delta G_s + \Delta G_v)$ model does not further fit the experimental data. It appears the contribution from ΔG_v is still overestimated because the fraction of the NS particles remaining intact was not considered. As a result, the addition of ΔG_s term shows a positive deviation compared with the experimental data.

4. Summary and conclusions

Two types of nanosilica (NS) fillers were evaluated as reinforcements and toughening agents for piperidine cured, epoxy resins. The addition of these well-dispersed NS particles did not significantly affect the T_g of the epoxy–silica nanocomposites (ESNs). As expected, the modulus of these filled epoxies increased with increasing NS content, which can be predicted by the Halpin–Tsai and simple series models. Interestingly, the compressive yield stress was found to be independent of NS content. In general, the compressive properties of 20 nm diameter NS-filled epoxies and 80 nm diameter NS-filled epoxies were nearly identical.

This study also demonstrated that nanosilica particle size has a negligible effect on improving fracture toughness of ESNs, at least in the NS-particle range of 20–80 nm in diameter. Note that the particle size is considered to be a critical factor in traditional micron size silica filled epoxies. The fracture toughness of ESNs increases with the NS volume fraction and no peak or plateau in fracture toughness is observed (up to 17.4 vol%). In addition, the matrix crosslink density affects the ability of the epoxy to plastically deform and high molecular weight between crosslinks is responsible for the high K_{IC} values obtained in this work.

Matrix plastic deformation plays an essential role in the zone shielding mechanism, which is credited for the toughening mechanisms in ESNs. The fracture surface and subsurface images demonstrate the presence of NS particle debonding, matrix ligament bridging, matrix dilation bands, and matrix shear banding. The use of Irwin's model describes the relationship between fracture toughness of ESNs and the plastic zone size reasonably well. The attempt of using shear banding and plastic void growth $(\Delta G_s + \Delta G_v)$ model proposed by Huang and Kinloch [47,48] was found to overestimate the amount of toughening observed. Much work remains in developing a more accurate model for predicting toughness in ESNs.

Acknowledgements

The authors are grateful for the generosity of 3M, Dow Chemical, and Nanoresins for providing their materials free of charge. The financial support from the Lehigh University/Mid-Atlantic Partnership (NASA co-op agreement No. NNX06AD01A) and the Semiconductor Research Corporation (Task 1292.027) are highly appreciated. A special thank goes to Dr. Gregory Hendricks at Core Electron Microscopy Facility, UMass Medical School for the TEM micrographs.

References

[1] Moloney AC, Kausch HH. J Mater Sci 1983;18:208–16.
[2] Moloney AC, Kausch HH. J Mater Sci 1984;19:1125–30.
[3] Lee J, Yee AF. Polymer 2000;41:8375–85.
[4] Lange FF, Radford KC. J Mater Sci 1971;6:1197–203.
[5] Kitey R, Tippur HV. Acta Mater 2005;53:1167–78.
[6] Zhang MQ, Rong MZ, Yu SL, Wetzel B, Friedrich K. Macromol Mater Eng 2002;287:111–5.
[7] Sprenger S, Eger C, Kinloch AJ, Lee JH, Taylor AC, Egan D. Special Issue of adhesion KLEBEN & DICHTEN; 2004, 3.
[8] Kinloch AJ, Lee JH, Taylor AC, Sprenger S, Eger C, Egan D. J Adhes 2003;79:867–73.
[9] Zhang H, Zhang Z, Friendrich K, Eger C. Acta Mater 2006;54:1833–42.
[10] Ragosta G, Abbate M, Musto P, Scarinzi G, Mascia L. Polymer 2005;46:10506–16.
[11] Kinloch AJ, Mohammed RD, Taylor AC, Eger C, Sprenger S, Egan D. J Mater Sci 2005;4:5083–6.
[12] Johnsen BB, Kinloch AJ, Mohammed RD, Taylor AC, Sprenger S. Polymer 2007;48:530–41.
[13] Rose LFR. Mech Mater 1987;6:11–5.
[14] Rose LFR. Int J Fract 1986;31:233–42.
[15] Lange FF. Philos Mag 1970;22:983–92.
[16] Odegard GM, Clancy TC, Gates TS. Polymer 2005;46:553–62.
[17] ASTM 1996;76:D695–6. 76–82.
[18] ASTM 1999;800:D5045–99. 800–08.
[19] Pearson RA. Ph. D. dissertation, Ann Arbor, MI: Michigan University; 1990 [chapter 2].
[20] Ferry JD. Viscoelastic properties of polymers. 3rd ed. New York: Wiley; 1980.
[21] Holik AS, Kambour RP, Hobbs SY, Fink DG. Microstruct Sci 1979;7:357–67.
[22] Pearson RA, Yee AF. J Appl Polym Sci 1993;48:1051–60.
[23] Yao XF, Yeh HY, Zhou D, Zhang YH. J Compos Mater 2006;40(4):371–81.
[24] Halpin JC, Tsai SW. Enviromental factors in composite materials design. AFML-TR67–423. Air Force Materials Laboratory; 1969.
[25] Halpin JC, Kardos JL. Polym Eng Sci 1976;16:344–52.
[26] Sperling LH. Introduction to physical polymer science. 4th ed. New Jersey: John Wiley & Sons, Inc.; 2006 [chapter 13].
[27] Ahmed S, Jones FR. J Mater Sci 1990;25:4933–42.
[28] Cho J, Joshi MS, Sun CT. Compos Sci Technol 2006;66:1941–52.
[29] Spanoudakis J, Young RJ. J Mater Sci 1984;19:473–86.
[30] Spanoudakis J, Young RJ. J Mater Sci 1984;19:487–96.
[31] Kawaguchi T, Pearson RA. Polymer 2003;44:4229–38.
[32] Amdouni N, Sautereau H, Gerard JF. J Appl Polym Sci 1992;46:1723–35.
[33] Kawaguchi T, Pearson RA. Polymer 2003;44:4239–47.
[34] Zhao S, Schadler SL, Hillborg H, Auletta T. Compos Sci Technol 2008;68:2976–82.
[35] Pearson RA, Yee AF. J Mater Sci 1989;24:2571–80.
[36] Kinloch AJ, Finch CA, Hashemi S. Polym Commun 1987;28:322–5.
[37] Kinloch AJ, Young RJ. Fracture behavior of polymers. London: Applied Science Publishers; 1983 [chapter 1].
[38] Kinloch AJ, Shaw SJ, Tod DA, Hunston DL. Polymer 1983;21:1341–54.
[39] Yee AF, Pearson RA. J Mater Sci 1986;21:2475–88.
[40] Lee J, Yee AF. Polymer 2001;42:577–88.
[41] Lee J, Yee AF. Polymer 2001;42:589–97.
[42] Kawaguchi T, Pearson RA. Compos Sci Technol 2004;64:1981–9.
[43] Kawaguchi T, Pearson RA. Compos Sci Technol 2004;64:1991–2007.
[44] Lazzeri A, Bucknall CB. J Mater Sci 1993;28:6799–808.
[45] Speroni F, Castoldi E, Fabbri P, Casiraghi T. J Mater Sci 1989;24:2165–76.
[46] Irwin GR. Proceedings of the 7th Sagamore Conference, Syracuse, NY, Syracuse University; 1960 (vol. II, 63).
[47] Huang Y, Kinloch AJ. J Mater Sci 1992;27:2753–62.
[48] Huang Y, Kinloch AJ. J Mater Sci 1992;27:2763–9.